University of Sistan and Baluchestan

Challenges in Nano and Micro Scale Science and Technology

Online ISSN: 2821 - 000X

Investigation of Friction Factor and Nusselt Number Distributions for Zno-water Nanofluid under Forced, Mixed and Free Convection with Varying Eckert Numbers

Tohid Adibi

Department of Mechanical Engineering, University of Bonab, Bonab, Iran .E-mail addresses: Tohidadibi@ubonab.ac.ir

Article Info

Article type:
Research Article

Article history:
Received: 05 April 2026
Received in revised form: 12 April 2026
Accepted: 26 April 2026
Published Online: 06 May 2026

Keywords:
Viscous Dissipation,
Nusselt Number,
Friction Factor,
Mixed Convection,
Free Convection

ABSTRACT

This study investigates the behavior of the friction factor and Nusselt number in fluid flow across forced, mixed, and free convection regimes, with a specific emphasis on the influence of the Eckert number. Numerical simulations were performed for a moving lid configuration, maintaining a constant Reynolds number (Re=100) while systematically varying the Grashof numbers ($Gr=10^3,10^4,10^5$) and Eckert numbers. The analysis reveals distinct trends: In forced ($Gr=10^3$) and mixed ($Gr=10^4$) convection, the mean friction factor remains largely constant across different Eckert numbers, while the mean Nusselt number shows a significant increase with Eckert number. This suggests that viscous dissipation primarily enhances heat transfer without substantially altering wall shear stress in these regimes. Conversely, under free convection ($Gr=10^5$), both mean friction factor and Nusselt number exhibit a substantial increase with rising Eckert number, highlighting the dominant role of buoyancy forces and viscous dissipation in governing both heat transfer and energy losses. Detailed friction factor distribution profiles further illustrate these phenomena, revealing unique behaviors, particularly the emergence of a near-zero slope region in free convection at higher Eckert numbers.

NOMENCLATURE

A	Area	Pr	Prandtl number
C	The volume fraction of nanoparticle	u, v	X, y velocity components
C_p	Specific heat in constant pressure (J/kg/K)	t	Time
f	Friction factor	U, v	Velocities
$\bar{f}$	Mean friction factor	x, y, r	Coordinates
Gr	Grashof number		**Greek symbols**
k	Thermal conductivity (W/m/K)	β	Thermal expansion coefficient (K^{-1})
M	Number of cells in x-direction	μ	Coefficient of viscosity (kg/m/s)
N	Number of cells in y-direction	ω	Rotational speed
Nc	Thermal conductivity parameter	υ	Kinematic viscosity (m^2/s)
Nu	Local Nusselt number	ρ	Density (kg/m^3)
$\overline{Nu}$	Mean Nusselt number	τ	Shear stress
Nv	Dynamic viscous parameter	∈	Artificial compressibility
P	Pressure		**Subscripts**
Re	Reynolds number	ref	Reference
Ri	Richardson	bf	Body fluid
T	Temperature	nf	Nano-fluid
		p	Particle

How to Cite this paper: Adibi T. Investigation of Friction Factor and Nusselt Number Distributions for Zno-water Nanofluid under Forced, Mixed and Free Convection with Varying Eckert Numbers. *Challenges in Nano and Micro Scale Science and Technology*. 2026; 14(2): 16-30. DOI: 10.22111/cnmst.2026.55029.1290

DOI: 10.22111/cnmst.2026.55029.1290

1. INTRODUCTION

In the realm of fluid dynamics and heat transfer, understanding the interplay between convection, viscous dissipation[1, 2], and flow characteristics is fundamental to numerous engineering applications[3, 4], ranging from microelectronic cooling systems[5, 6] to energy generation processes[7, 8]. The Eckert number, a dimensionless parameter representing the ratio of kinetic energy to enthalpy, plays a critical role in quantifying the significance of viscous dissipation[9-11], which can act as an internal heat source within the fluid. Analyzing phenomena such as the Nusselt number (a measure of convective heat transfer) and the friction factor (indicating resistance to flow) under various conditions, including forced, mixed, and free convection, provides crucial insights into system efficiency and performance[12-14]. This review aims to synthesize existing research on these parameters, exploring how variations in the Eckert number and dominant convection modes influence thermal and hydrodynamic behaviors, thereby establishing a foundation for our current investigation into these complex interactions.

Hedayati and Ramiar [15] presented an unsteady, two-phase simulation of nanofluid behavior within a system of moving parallel plates, incorporating the influence of a magnetic field. Our model accounts for key nanofluid dynamics, specifically thermophoresis and Brownian motion. The governing equations were solved concurrently using the Galerkin method, a technique validated against existing literature for its suitability in similar problems. A semi-analytical approach was employed to examine the effects of several critical parameters, including the squeeze number, Eckert number, and Hartmann number. Key findings reveal that the skin friction coefficient increases with higher Hartmann and squeeze numbers when the Reynolds number is held constant. Furthermore, the Nusselt number demonstrates a positive correlation with the Hartmann number, while the Eckert number exhibits a decreasing relationship with the squeeze number. These insights are expected to aid engineers in design optimization and facilitate more efficient research investigations. Ibrahim et al. [16] analyzed heat and mass transfer in unsteady MHD flow of a micropolar fluid over a porous stretching sheet with chemical reaction. Using similarity transformations and a fourth-order Runge-Kutta method, the research numerically solves governing PDEs. Results are presented graphically and in tables, showing the influence of various parameters on fluid behavior and transfer rates. Khorasanizadeh et al. [17] numerically investigated convective heat transfer enhancement in a partitioned square cavity using water-SiO2 nanofluid. It analyzes the impact of SiO2 nanoparticle concentration (2-4%) and shape (blades, platelets, cylindrical, bricks, spherical) on fluid flow and heat transfer. The study, using the finite-volume method and SIMPLE algorithm, explores parameters like Rayleigh number and partition height. Results show that streamlines and isotherms are significantly affected by Rayleigh number and partition height, with average Nusselt number increasing as Rayleigh number rises for a fixed partition height. Shahriari et al.[18] examined natural convection heat transfer of CuO-water nanofluid in a wavy-walled cavity under a uniform magnetic field using the lattice Boltzmann model. The left wall is sinusoidally heated, the right wall is kept at a constant cold temperature, and the top/bottom walls are insulated. The study investigates parameters like nanoparticle volume fraction (φ), Rayleigh number (Ra), Hartmann number (Ha), and phase deviation (Φ). Key findings indicate that heat transfer decreases with increasing Hartmann number but increases with higher Rayleigh number and nanoparticle volume fraction. The magnetic field amplifies the nanoparticles' effect at Ra = 10^4 and 10^5 compared to Ra = 10^3. The most significant nanoparticle effects are observed with varying phase deviations as the Rayleigh number increases. This research offers insights for improving MHD natural convection heat transfer in wavy-walled cavities with sinusoidal temperature distributions. Arani et al. [19] numerically investigated mixed convection fluid flow and heat transfer of water-Al2O3 nanofluid within a lid-driven square cavity. The study focuses on finding the optimal distribution of discrete heat sources on the cavity wall. The researchers examined the effects of heat source length, Richardson number (Ri), and Grashof number (Gr) on the optimal heat source location. They also compared the average Nusselt number for nanofluids modeled with both constant and variable properties.

Sharma et al. [20] examined the steady two-dimensional flow of a hybrid nanofluid over an exponentially expanding/shrinking surface under a magnetic field, with thermal buoyancy effects included. Using similarity transformation and the Runge–Kutta fourth-order method, the governing equations are solved numerically, revealing a dual solution for certain parameters. Notably, increasing nanoparticle volume fraction enhances velocity in the first solution but reduces it in the second, highlighting the complex, non-monotonic behavior of hybrid nanofluids in such flows. In other work, they [21] investigated the two-dimensional incompressible flow of a Williamson nanofluid induced by an inclined, infinite, expanding/contracting cylinder at an angle to the horizontal. The analysis focuses on the non-Newtonian behavior of the fluid and its influence on heat and mass transfer characteristics. The governing partial differential equations are transformed into dimensionless form and solved numerically using a shooting-based Runge–Kutta fourth-order method. Key findings reveal that suction reduces fluid velocity ,while injection significantly enhances it ,demonstrating opposite effects on the flow dynamics. The impact of various parameters—such as the Williamson parameter, inclination angle, suction/injection, and nanoparticle concentration—is analyzed through graphical and tabular results, highlighting their roles in altering velocity, temperature, and concentration profiles. The study provides valuable insights into the complex behavior of non-Newtonian nanofluids in industrial applications involving inclined surfaces, such as polymer extrusion, wire coating, and cooling processes, where precise control of flow and heat transfer is essential.

Iqbal et al. [22] investigated hybrid nanofluids (water-ethylene glycol with Al2O3 and Fe3O4) over a thin needle under an inclined magnetic field. Using Runge-Kutta methods, results show Al2O3 offers slightly higher heat transfer and drag than Fe3O4. The research analyzes velocity, entropy generation, and the Bejan number, highlighting applications in needle systems. Razavi et al. [23] investigated fin configurations for natural gas preheating to prevent hydrates. Using 3D simulations in FORTRAN, it analyzed solid/interrupted fins with longitudinal/circular arrangements and various cross-sections. Results indicate that increasing fin count boosts heat transfer, while higher fin-to-diameter ratios reduce it. Notably, divergent parabolic fins yielded the most significant heat transfer improvement. Adibi et al. [24] numerically investigated forced, free, and mixed convection using Al2O3, TiO2, MgO, and ZnO-water nanofluids. Simulations of cavity and cylinder flows, developed in FORTRAN 95, reveal that MgO-water yields the highest heat transfer (15–37% increase), while ZnO-water shows the lowest. Additionally, Al2O3-water and TiO2-water exhibited the maximum and minimum shear stresses, respectively.

This study examines the steady two-dimensional flow of a hybrid nanofluid over an exponentially expanding/shrinking surface under a magnetic field, with thermal buoyancy effects included. Using similarity transformation and the Runge–Kutta fourth-order method, the governing equations are solved numerically, revealing a dual solution for certain parameters. Notably, increasing nanoparticle volume fraction enhances velocity in the first solution but reduces it in the second, highlighting the complex, non-monotonic behavior of hybrid nanofluids in such flows.

This study contributes a novel analysis by focusing on the distinct, and sometimes contrasting, impacts of viscous dissipation (as modulated by the Eckert number) on heat transfer and fluid friction across forced, mixed, and particularly free convection regimes. While previous works have often examined these factors in isolation or under simplified conditions, our comprehensive review and subsequent analysis reveal a nuanced dependency, especially highlighting the amplified effects of viscous dissipation in free convection scenarios. The findings offer significant practical implications for the design and optimization of thermal systems where viscous heating is a dominant factor, such as in high-speed lubrication systems, microfluidic devices with significant shear rates, or advanced cooling technologies. By elucidating these complex correlations, this research provides engineers and designers with a more refined understanding to enhance efficiency, predict performance, and mitigate potential thermal management challenges in these critical applications.

2. METHODOLOGY

In the analysis of fluid-flow phenomena, the behavior of a continuum is described through a set of differential equations representing the conservation of mass, momentum, and energy. These equations, derived from fundamental principles of fluid mechanics and thermodynamics, provide a unified framework for predicting the spatial and temporal evolution of velocity, pressure, and temperature fields. The continuity equation enforces mass conservation within a control volume, ensuring consistency between density variations and mass fluxes. The momentum equations in the three coordinate directions characterize the response of the fluid to surface and body forces such as pressure, viscosity, and gravity, thereby defining the dynamic structure of the flow. Complementing these, the energy equation accounts for heat transfer, work interactions, and thermodynamic effects, enabling the assessment of temperature distributions and convective transport mechanisms. Together, these governing equations form the basis of analytical and numerical modeling in fluid dynamics.

The following assumptions are made to simplify and analyze the fluid flow and heat transfer phenomena:

1. The fluid is assumed to be incompressible. This assumption is justified due to the low flow velocities, significantly below Mach 0.3.
2. The fluid is considered Newtonian. The properties of the base fluid (water) are updated considering the addition of ZnO nanoparticles at a volume fraction of 3%, based on established correlations from the literature.
3. The flow is initially described in three-dimensional Cartesian coordinates and subsequently simplified to two-dimensional for the numerical simulations.
4. The flow is assumed to be in a steady state for the physical analysis. However, for numerical convergence, the governing equations were solved transiently until a steady-state solution was reached.
5. There is no heat source located within the cavity.
6. The velocity of the top moving lid is considered constant.
7. The temperatures of the top and bottom plates are assumed to be constant.
8. The side walls of the cavity are assumed to be adiabatic and stationary.

To begin our detailed analysis, we first present the mathematical formulation for mass conservation. Specifically, for a three-dimensional flow of an incompressible Newtonian fluid described in Cartesian coordinates, the continuity equation takes the following form[25]:

$$\left(\frac{\partial u}{\partial x}+\frac{\partial v}{\partial y}+\frac{\partial w}{\partial z}\right)=0 \tag{1}$$

Having established the conservation of mass, the next crucial step is to describe the forces acting on the fluid and their effect on its acceleration. This is captured by the momentum equations. For our three-dimensional flow scenario, these equations, derived from Newton's second law applied to a fluid element, are presented below[25]:

$$\rho\left(\frac{\partial u}{\partial t}+u\frac{\partial u}{\partial x}+v\frac{\partial u}{\partial y}+w\frac{\partial u}{\partial z}\right)=\rho g_x-\frac{\partial p}{\partial x}+\mu\left(\frac{\partial^2 u}{\partial x^2}+\frac{\partial^2 u}{\partial y^2}+\frac{\partial^2 u}{\partial z^2}\right) \tag{2}$$

$$\rho\left(\frac{\partial v}{\partial t}+u\frac{\partial v}{\partial x}+v\frac{\partial v}{\partial y}+w\frac{\partial v}{\partial z}\right)=\rho g_y-\frac{\partial p}{\partial y}+\mu\left(\frac{\partial^2 v}{\partial x^2}+\frac{\partial^2 v}{\partial y^2}+\frac{\partial^2 v}{\partial z^2}\right) \tag{3}$$

$$\rho\left(\frac{\partial w}{\partial t}+u\frac{\partial w}{\partial x}+v\frac{\partial w}{\partial y}+w\frac{\partial w}{\partial z}\right)=\rho g_z-\frac{\partial p}{\partial z}+\mu\left(\frac{\partial^2 w}{\partial x^2}+\frac{\partial^2 w}{\partial y^2}+\frac{\partial^2 w}{\partial z^2}\right) \tag{4}$$

Finally, to provide a complete thermodynamic description of the fluid flow, we incorporate the energy equation. This equation accounts for the conservation of energy within the fluid system, and crucially for our subsequent analysis, it explicitly includes the term for viscous dissipation, which represents the irreversible conversion of mechanical energy into thermal energy due to fluid friction[25]:

$$\frac{\partial T}{\partial t}+u\frac{\partial T}{\partial x}+v\frac{\partial T}{\partial y}+w\frac{\partial T}{\partial z}=\frac{1}{\rho C_p}\left(u\frac{\partial p}{\partial x}+v\frac{\partial p}{\partial y}+w\frac{\partial p}{\partial z}\right)+\frac{k}{\rho C_p}\left(\frac{\partial^2 T}{\partial x^2}+\frac{\partial^2 T}{\partial y^2}+\frac{\partial^2 T}{\partial z^2}\right)+\frac{\mu}{\rho C_p}\Phi \tag{5}$$

$$\Phi=\left(\frac{\partial u}{\partial y}+\frac{\partial v}{\partial x}\right)^2+\left(\frac{\partial u}{\partial z}+\frac{\partial w}{\partial x}\right)^2+\left(\frac{\partial v}{\partial z}+\frac{\partial w}{\partial y}\right)^2+2\left(\left(\frac{\partial u}{\partial x}\right)^2+\left(\frac{\partial v}{\partial y}\right)^2+\left(\frac{\partial w}{\partial z}\right)^2\right) \tag{6}$$

Given the geometric constraints and the nature of the flow, we now proceed to simplify the governing equations by neglecting the variations in the third dimension. This reduction leads to a two-dimensional formulation, which effectively captures the essential physics of the problem while significantly simplifying the computational requirements:

$$\frac{\partial u}{\partial x}+\frac{\partial v}{\partial y}=0 \tag{7}$$

$$\frac{\partial u}{\partial t}+u\frac{\partial u}{\partial x}+v\frac{\partial u}{\partial y}=-\frac{1}{\rho}\frac{\partial p}{\partial x}+\upsilon\left(\frac{\partial^2 u}{\partial x^2}+\frac{\partial^2 u}{\partial y^2}\right) \tag{8}$$

$$\frac{\partial v}{\partial t}+u\frac{\partial v}{\partial x}+v\frac{\partial v}{\partial y}=-g-\frac{1}{\rho}\frac{\partial p}{\partial y}+\upsilon\left(\frac{\partial^2 v}{\partial x^2}+\frac{\partial^2 v}{\partial y^2}\right) \tag{9}$$

$$\frac{\partial T}{\partial t}+u\frac{\partial T}{\partial x}+v\frac{\partial T}{\partial y}=\frac{1}{\rho C_p}\left(u\frac{\partial p}{\partial x}+v\frac{\partial p}{\partial y}\right)+\frac{k}{\rho C_p}\left(\frac{\partial^2 T}{\partial x^2}+\frac{\partial^2 T}{\partial y^2}\right)+\frac{\mu}{\rho C_p}\Phi \tag{10}$$

$$\Phi=\left(\frac{\partial u}{\partial y}+\frac{\partial v}{\partial x}\right)^2+2\left(\left(\frac{\partial u}{\partial x}\right)^2+\left(\frac{\partial v}{\partial y}\right)^2\right) \tag{11}$$

To facilitate a more general analysis and to identify the key dimensionless parameters governing the fluid flow, we will now non-dimensionalize the governing equations. This process involves scaling the relevant variables by characteristic quantities and reveals the relative importance of different physical phenomena through dimensionless numbers such as the Reynolds, Prandtl, Grashof, Richardson, and Eckert numbers:

Using continuity equation we have:

$$u\left(\frac{\partial u}{\partial x}+\frac{\partial v}{\partial y}\right)=0,\ v\left(\frac{\partial u}{\partial x}+\frac{\partial v}{\partial y}\right)=0,\ T\left(\frac{\partial u}{\partial x}+\frac{\partial v}{\partial y}\right)=0 \tag{12}$$

using equations (8) and (12) results in:

$$u\left(\frac{\partial u}{\partial x}+\frac{\partial v}{\partial y}\right)+\frac{\partial u}{\partial t}+u\frac{\partial u}{\partial x}+v\frac{\partial u}{\partial y}=-\frac{1}{\rho}\frac{\partial p}{\partial x}+\upsilon\left(\frac{\partial^2 u}{\partial x^2}+\frac{\partial^2 u}{\partial y^2}\right) \tag{13}$$

So, we have:

$$\frac{\partial u}{\partial t}+2u\frac{\partial u}{\partial x}+u\frac{\partial v}{\partial y}+v\frac{\partial u}{\partial y}=-\frac{1}{\rho}\frac{\partial p}{\partial x}+\upsilon\left(\frac{\partial^2 u}{\partial x^2}+\frac{\partial^2 u}{\partial y^2}\right) \tag{14}$$

Then:

$$\frac{\partial u}{\partial t}+\frac{\partial (u^2)}{\partial x}+\frac{\partial (uv)}{\partial y}=-\frac{1}{\rho}\frac{\partial p}{\partial x}+\upsilon\left(\frac{\partial^2 u}{\partial x^2}+\frac{\partial^2 u}{\partial y^2}\right) \tag{15}$$

Then:

$$\frac{\partial u}{\partial t}+\frac{\partial\left(u^2+\frac{1}{\rho}p\right)}{\partial x}+\frac{\partial (uv)}{\partial y}=\upsilon\left(\frac{\partial^2 u}{\partial x^2}+\frac{\partial^2 u}{\partial y^2}\right) \tag{16}$$

And finally, the dimensionless form of governing equation is obtained as

$$\frac{\partial Q}{\partial t}+\frac{\partial F}{\partial x}+\frac{\partial G}{\partial y}=\frac{\partial R}{\partial x}+\frac{\partial S}{\partial y}+H \tag{17}$$

$$\vec{Q}=\begin{bmatrix} p\\ u\\ v\\ T\end{bmatrix},\quad F=\begin{bmatrix} \beta u\\ p+u^2\\ uv\\ (T-Ec\,p)u\end{bmatrix},\quad G=\begin{bmatrix} \beta v\\ uv\\ p+v^2\\ (T-Ec\,p)v\end{bmatrix},\quad R=\frac{1}{\mathrm{Re}}\begin{bmatrix} 0\\ \frac{\partial u}{\partial x}\\ \frac{\partial v}{\partial x}\\ \frac{1}{\mathrm{Pr}}\frac{\partial T}{\partial x}\end{bmatrix},$$

$$S=\frac{1}{\mathrm{Re}}\begin{bmatrix} 0\\ \frac{\partial u}{\partial y}\\ \frac{\partial v}{\partial y}\\ \frac{1}{\mathrm{Pr}}\frac{\partial T}{\partial y}\end{bmatrix},\quad H=\begin{bmatrix} 0\\ 0\\ \frac{Gr}{\mathrm{Re}^2}T\\ \frac{Ec}{\mathrm{Re}}\Phi\end{bmatrix},\quad \Phi=\left(\frac{\partial u}{\partial y}+\frac{\partial v}{\partial x}\right)^2+2\left(\left(\frac{\partial u}{\partial x}\right)^2+\left(\frac{\partial v}{\partial y}\right)^2\right), \tag{18}$$

Equations 17 and 18 are nondimensionalized using equation 19, and for simplicity, the asterisk notation has been omitted from all nondimensional variables. The pressure is scaled in such a way that the gravitational body force is eliminated in the nondimensional form. In other words, the gravitational term is first incorporated into the pressure to obtain the modified (or hydrostatic) pressure, and this resulting pressure is then nondimensionalized.

$$u^*=\frac{u}{U_{ref}},\ v^*=\frac{v}{U_{ref}},\ x^*=\frac{x}{L_{ref}},\ y^*=\frac{y}{L_{ref}},\ p^*=\frac{p+\rho g y-p_\infty}{\rho_{ref}U_{ref}^2},\ t^*=\frac{tU_{ref}}{L_{ref}},\ T^*=\frac{T-T_{ref1}}{T_{ref2}-T_{ref1}} \tag{19}$$

To nondimensionalize the temperature field, two reference temperatures are used. The first reference temperature T_{ref2} is taken as the bottom-wall temperature, leading to a nondimensional value of $T^*=+1$ at the lower plate. The second reference temperature T_{ref1} is defined as the arithmetic mean of the temperatures of the upper and lower walls. Under this definition, the nondimensional temperature of the top plate becomes $T^*=-1$. This symmetric scaling is commonly employed in mixed and natural convection studies and facilitates the interpretation of the temperature distribution.

The pressure is nondimensionalized according to $p^*=\frac{p+\rho g y-p_\infty}{\rho_{ref}U_{ref}^2}$, which removes the hydrostatic contribution and ensures that only dynamic pressure variations appear in the governing equations. This scaling was also used in the authors' previous work[26, 27].The velocity components are scaled by the top-wall velocity U_{ref}, the spatial coordinates by the cavity width L, and the time by L/U_{ref}, so that the nondimensional equations preserve a form similar to the dimensional Navier–Stokes and energy equations.

In our earlier works[27, 28], the thermal boundary conditions were considered in the opposite configuration, i.e., the top wall was assumed hot while the bottom wall was assumed cold, so the buoyancy-driven flow mechanism was correspondingly different. In the present study, we intentionally changed the boundary conditions to the configuration with a heated bottom wall and a cold moving lid in order to clearly examine and quantify the resulting buoyancy effects. In particular, this modification enables us to investigate how the system behaves when the heated fluid near the bottom becomes less dense and tends to rise, while the colder fluid (with higher density) tends to occupy the upper region to satisfy continuity. Therefore, the present results specifically reveal the impact of buoyancy-force orientation on both the flow structure and the associated heat transfer characteristics.

The dimensionless numbers governing the flow behavior are introduced in Equation 18. These include the Reynolds number (Re), Prandtl number (Pr), Eckert number (Ec), and Grashof number (Gr), which are defined by the following relations:

$$Re = \frac{\rho_{ref} u_{ref} L_{ref}}{\mu}, Pr = \frac{c_P \mu}{k}, \ Ec = \frac{u_{ref}^2}{c_P(T_{ref2} - T_{ref1})}, \ Gr = \frac{\beta_{ex}\, g(T_{ref2} - T_{ref1}) L_{ref}^3}{\upsilon^2} \quad (20)$$

The governing equations have been discretized using the Finite Volume Method (FVM), a robust numerical technique particularly well-suited for conservation laws. FVM divides the computational domain into a finite number of control volumes (cells) and enforces conservation principles over each volume. By integrating the vector form of the governing equation (18) over a typical cell surface, we obtain the following discretized equation:

$$\frac{\partial}{\partial t}\iint Q dA + \iint \left(\frac{\partial(F-R)}{\partial x} + \frac{\partial(G-S)}{\partial y}\right) = \iint H dA \quad (21)$$

Green's theorem provides a mathematical framework for converting area (or volume) integrals of divergence terms into line or surface integrals over the boundary of a control volume. This transformation is central to the Finite Volume Method, as it allows fluxes across the cell faces to be expressed explicitly in terms of boundary quantities. After applying Green's theorem and converting the volume integral over the cell to a closed surface integral over its boundaries, the following relation is obtained.

$$\frac{\partial}{\partial t}\iint Q dA + \oint((F-R)\, dy - (G-S) dx) = \iint H dA \quad (22)$$

Discretizing the resulting equation for a two-dimensional domain with quadrilateral cells leads to the following algebraic expression:

$$A_{ij}\frac{\partial Q_{ijk}}{\partial t} = \left[\sum_{m=1}^{4}\left((F_{ijk} - R_{ijk})\Delta y - (G_{ijk} - S_{ijk})\Delta x\right)_m - A_{ij} H_{ijk}\right], k = 1,2,3,4 \quad (23)$$

To accurately capture the convective and viscous transport phenomena, a staggered discretization approach is employed. Convective terms are treated using a second-order accurate averaging scheme, which minimizes numerical diffusion and preserves the sharpness of gradients. For the viscous terms, a fourth-order accurate averaging scheme is utilized. This higher-order scheme is particularly important for accurately resolving the viscous stresses, which often vary significantly in complex flow fields. Temporal discretization is achieved through a robust fourth-order Runge-Kutta method. This explicit time-stepping scheme offers a good balance between accuracy and computational efficiency, allowing for stable and precise integration of the governing equations over time, while minimizing time-truncation errors.

3. RESULT AND DISCUSSION

The discussion and results section of this paper is dedicated to presenting and analyzing the numerical simulations performed to investigate the impact of viscous dissipation, quantified by the Eckert number, on various flow and thermal characteristics. Prior to the detailed parametric study, crucial steps of grid independence verification and code validation were undertaken to ensure the reliability and accuracy of the obtained results. Grid independence was systematically assessed by refining the computational mesh and comparing key output parameters, such as velocity profiles and Nusselt numbers, to confirm that the solution is not significantly affected by the grid resolution. Subsequently, the computational code was validated against established benchmark solutions for similar flow configurations. This validation process involved comparing our numerical predictions with experimentally measured or analytically derived data, confirming the code's capability to accurately replicate the underlying physics of the problem.

Following the confirmation of grid independence and code validation, a systematic investigation was conducted to elucidate the role of the Eckert number across different flow regimes. The study systematically explores three distinct scenarios: forced convection ($Re=10^2$, $Gr=10^3$), mixed convection ($Re=10^2$, $Gr=10^4$), and natural convection ($Re=10^2$, $Gr=10^5$). For each regime, simulations were performed across a range of varying Eckert numbers. The outcomes of these simulations are presented and analyzed, focusing on velocity profiles, temperature distributions, and streamline patterns to visualize the flow behavior. Furthermore, quantitative metrics, namely the Nusselt number and friction factor, were calculated for each Eckert number and flow regime. These results are graphically represented and compared to highlight the evolving influence of viscous dissipation under different convective conditions.

The nondimensional viscous dissipation term Φ was verified to be correctly scaled in the dimensionless energy equation. Although viscous dissipation is often assumed to be small for many flow configurations, its relative importance depends on the combined effects of viscosity, characteristic velocity, and imposed temperature differences. Since these parameters can vary widely in different applications, the assumption of negligible Φ is not universally justified. In the present study, the choice of Re=100 and Ec=1 highlights a regime in which viscous dissipation can have a non-trivial contribution to the temperature field, emphasizing that this term should not always be omitted a priori.

The computational domain consists of a two-dimensional square cavity with dimensions of 1x1 unit. The simulation models the fluid dynamics and heat transfer within this cavity. The top wall of the cavity is set in motion towards the right, representing an external forcing mechanism, while the remaining three walls (bottom and both vertical sides) are held stationary. The working fluid considered for this study is a ZnO-Water nanofluid. For consistency and ease of analysis across different physical scales, all relevant parameters, including velocity, temperature, and fluid properties, are treated in a dimensionless form.

The thermal boundary conditions are specified as follows: the top moving wall is maintained at a constant cold temperature ($T_{top}=-1$), the stationary bottom wall is kept at a constant hot temperature ($T_{bottom}=+1$), and the vertical side walls are designated as adiabatic, implying zero heat flux across them. The no-slip condition for velocity is imposed on all solid boundaries, ensuring that the fluid velocity matches the wall velocity at the interface. For temperature, the no-penetration condition is applied to the adiabatic side walls, meaning the temperature gradient normal to these walls is set to zero ($\partial T/\partial n=0$), which mathematically represents the adiabatic nature of these boundaries. The pressure boundary condition on the walls is determined using a second-order extrapolation. The initial conditions for velocity, temperature, and pressure throughout the cavity are set to zero. The simulation is iterated until the residuals for all governing equations fall below a convergence criterion of 10^{-5}, ensuring a steady-state or sufficiently converged solution.

The use of nanofluids has garnered significant attention in recent years due to their enhanced thermal properties compared to conventional base fluids. Nanofluids, which are stable suspensions of nanoparticles in a base fluid, offer superior thermal conductivity, convective heat transfer coefficients, and increased specific heat capacity. These enhanced characteristics make them highly promising for a variety of heat transfer applications, including but not limited to, solar collectors, heat exchangers, and microelectronics cooling. For this study, a ZnO-Water nanofluid was selected owing to its well-documented thermophysical properties and its demonstrated efficacy in improving heat transfer performance. The specific thermophysical properties of the ZnO-Water nanofluid employed in this simulation, including thermal conductivity, viscosity, and specific heat, were carefully extracted from the established literature, specifically referencing the findings detailed in [24].

Error plots are fundamental in numerical simulations as they provide crucial insights into the convergence, stability, and accuracy of the employed numerical methods. They visually represent how the residual error decreases over iterations or steps, serving as a primary indicator of whether the solution is approaching a steady state or a desired level of precision. Analyzing the error plot allows researchers to validate the numerical scheme, identify potential issues such as oscillations, slow convergence, or divergence, and confirm that the chosen parameters (like time step size or grid resolution) are appropriate for the problem at hand. Ultimately, a well-behaved error plot is essential for establishing confidence in the obtained numerical results.

The error plot you described for Gr = 1000 and Gr = 10000 demonstrates the solver's progression towards a converged solution. The observed decrease in error from approximately 10^{-1} to 10^{-5} indicates that the numerical solver successfully captured the underlying physics and reached a satisfactory level of accuracy in both cases. Notably, the convergence was achieved more rapidly for Gr = 1000, suggesting that the flow regime at this Grashof number was less complex or inherently more stable for the numerical method. The oscillatory nature of the plot, with local minima and maxima, is characteristic of simulations involving strong buoyancy effects. This oscillation signifies the solver's iterative process of adjusting to the developing flow structures, where localized improvements in accuracy might be followed by slight increases in error as the solution adapts to new flow patterns before ultimately settling towards the overall descending trend. This behavior, despite its fluctuations, confirms the solver's ability to handle these challenging flow conditions.

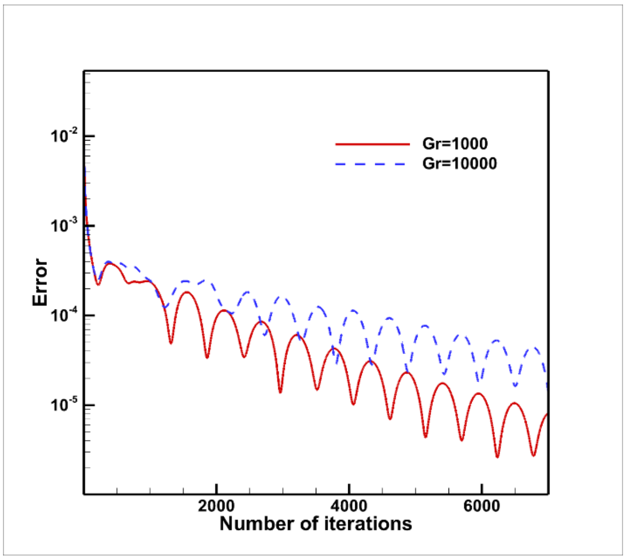

Fig. 1. Convergence Behavior of the Numerical Solver for High Grashof Numbers (Gr = 1000 and 10000)

Grid independence is a fundamental requirement in numerical simulations, as it ensures that the predicted results are not significantly influenced by the discretization of the computational domain. A properly conducted grid independence study increases the reliability and credibility of the simulation results by demonstrating that the solution has reached a level of numerical convergence. In other words, it confirms that further mesh refinement does not lead to meaningful changes in the key flow variables. This step is especially important in fluid dynamics problems, where inaccurate mesh resolution may distort local gradients, boundary-layer behavior, and overall flow characteristics. Therefore, performing a grid independence analysis is essential before presenting final numerical results.

A grid independence study was performed to verify the adequacy of the numerical mesh. Simulations were carried out using three different mesh densities, consisting of 22,500, 62,500, and 160,000 elements. The results were evaluated in terms of the horizontal velocity variation along the cavity centerline. Comparison of the obtained profiles showed that the difference between the two finer meshes was less than 0.5%, indicating that further mesh refinement has a negligible effect on the solution. Based on this observation, the mesh with 62,500 elements was selected as the final grid for all subsequent simulations due to its balance between numerical accuracy and computational efficiency.

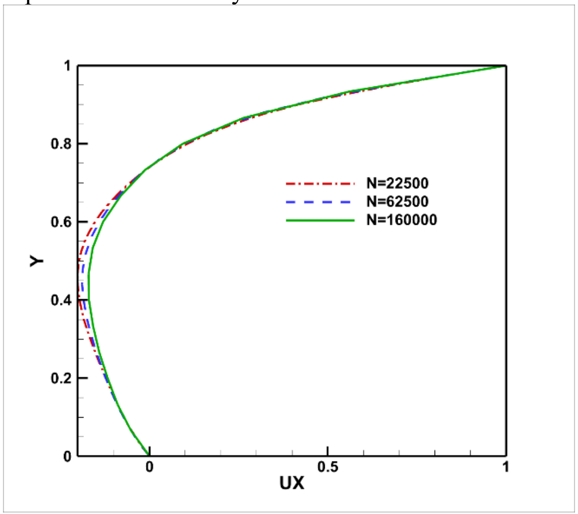

Fig. 2. Grid independence study based on horizontal velocity along the cavity centerline

Validation is a critical step in any numerical study, as it establishes the credibility and reliability of the computational model. By comparing simulation results with established experimental or numerical data from the literature, validation demonstrates that the mathematical model, boundary conditions, and numerical methods are capable of accurately predicting the physical phenomena under study. Without proper validation, numerical results may be questionable, and their application to more complex or novel configurations would lack a solid foundation. Thus, validation serves as a benchmark that confirms the code is working correctly and the predicted results are trustworthy.

To validate the present numerical model, the vertical velocity profiles along the cavity centerline obtained from the current simulation were compared with the results reported by Iwatsu et al. [29], a well-established study in this field. Figure 3 shows the comparative analysis, which demonstrates excellent agreement between the present results and the reference data. The maximum relative deviation between the two datasets was found to be less than 0.3%, indicating that the numerical method and the mesh configuration employed in this study are sufficiently accurate. This close match confirms that the current code is correctly capturing the flow physics and provides confidence in the reliability of the subsequent simulation results.

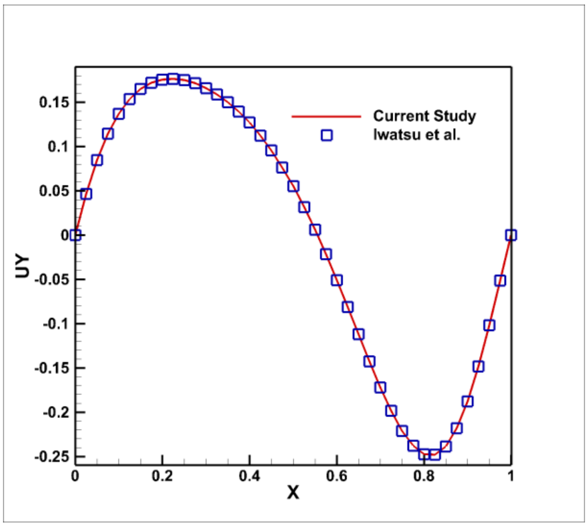

Fig. 3. Validation of current study with that of Iwatsu et al. [29] based on vertical velocity along the cavity centerline

The velocity contours presented in Figure 4 illustrate the horizontal and vertical velocity fields of the ZnO–water nanofluid within the square cavity for two Eckert numbers, Ec = 0 and Ec = 1. The horizontal velocity contours range from −0.2 to 1.0, which is fully consistent with the boundary conditions: the top wall moves to the right with a nondimensional velocity of 1 while the other three walls remain stationary. As expected, regions close to the moving lid exhibit velocities approaching 1, while zones where the flow recirculates toward the left display negative velocities. The magnitude of the negative velocity is larger in the central region compared to the lower region, consistent with the no-slip condition that forces the velocity to diminish toward zero near the bottom wall. Increasing the Eckert number induces only minor changes in the horizontal velocity distribution, indicating that viscous dissipation has a limited influence on the primary flow structure at the specified Reynolds and Grashof numbers.

The vertical velocity contours, spanning from approximately −0.45 to 0.3, further validate the expected behavior of the cavity flow. The velocity component in the vertical direction approaches zero near all solid boundaries due to the no-slip condition. In the left half of the cavity, the vertical velocity is predominantly positive, reflecting upward motion associated with the main circulation cell. Conversely, negative vertical velocities appear on the right side as the flow moves downward to complete the recirculation loop. This pattern is characteristic of lid-driven cavity flows influenced by buoyancy forces. Similar to the horizontal component, the effect of increasing the Eckert number on the vertical velocity field is modest, indicating that the thermal-to-mechanical energy conversion through viscous dissipation does not substantially alter the overall flow topology under the examined conditions.

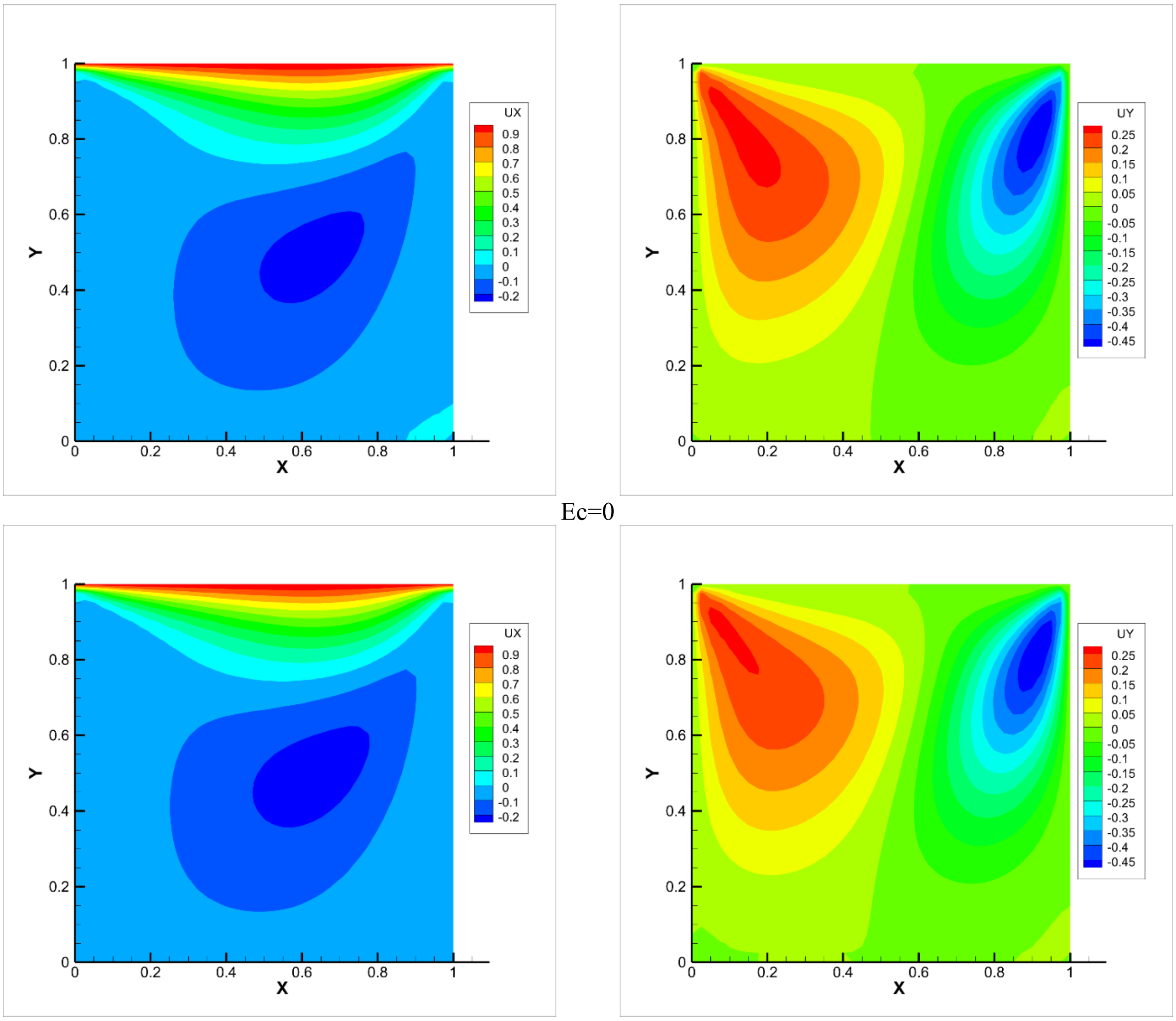

Fig. 4. The effect of Eckert number on horizontal and vertical velocity contour at Re=100, Gr=1000

The temperature contours in Figure 5 illustrate the influence of the Eckert number on the thermal field under both forced and free convection regimes. In the upper subfigures (Re = 100, Gr = 1000), the temperature varies between −1 at the top wall and +1 at the bottom wall, and the isotherms remain perpendicular to the adiabatic vertical walls due to the zero heat flux condition. Increasing the Eckert number from 0 to 1 leads to a noticeable—but not drastic—elevation of temperature in several regions, indicating mild heating of the nanofluid due to viscous dissipation. Although local temperatures increase (for example, a region previously at $\theta = 0.2$ may rise to about $\theta = 0.5$), the minimum and maximum temperatures remain fixed at the boundaries because the physical boundary conditions enforce the same temperature limits. Given that the Richardson number for these cases is approximately $Ri = Gr/Re^2 = 0.1$, the flow regime is dominated by forced convection, which explains why the Eckert number has only a limited impact on the overall temperature distribution.

A markedly different behavior is observed in the lower subfigures corresponding to Gr = 100000, where the Richardson number increases to Ri = 10, indicating strong free convection dominance. In the case of Ec = 0, the temperature still lies between −1 and +1; however, the penetration of thermal boundary layers into the cavity is weaker, resulting in a large region of nearly isothermal fluid with temperatures close to zero. This is characteristic of buoyancy-driven circulation in which strong flow recirculation mixes the fluid and tends to homogenize the temperature field. When the Eckert number is increased to Ec = 1, the thermal field changes dramatically: the maximum temperature reaches values as high as $\theta \approx 2.5$, meaning that viscous dissipation generates substantial additional heating. This heating becomes especially significant when buoyancy is strong, because the intensified recirculation redistributes the internally generated heat throughout the cavity.

Overall, Figure 5 demonstrates that the influence of the Eckert number is strongly dependent on the flow regime. Under forced convection (Ri = 0.1), viscous heating contributes only minor thermal variations, leaving the global temperature bounds unchanged. In contrast, under free convection (Ri = 10), the enhanced buoyancy forces amplify the effect of viscous dissipation, leading to a pronounced rise in maximum temperature far beyond the boundary-imposed limits. This highlights the nonlinear coupling between viscous heating and buoyancy-driven flow, showing that even moderate viscous dissipation can significantly reshape the thermal structure when natural convection dominates.

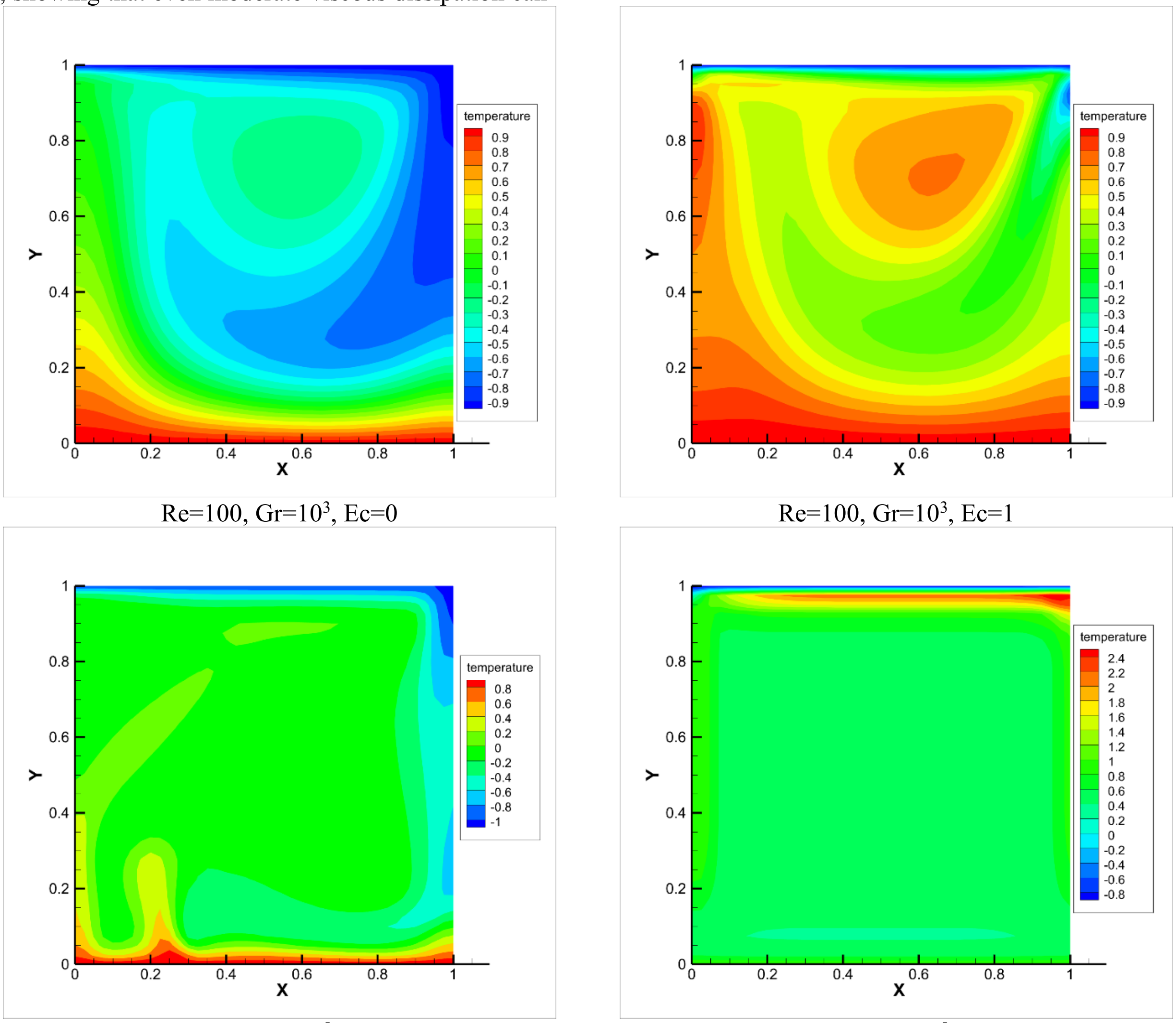

Re=100, Gr=10^3, Ec=0 Re=100, Gr=10^3, Ec=1

Re=100, Gr=10^5, Ec=0 Re=100, Gr=10^5, Ec=1

Fig. 5. The effect of Eckert number on temperature contour at forced and free convection

The dimensionless shear stress and friction factor is computed by the following relation.

$$f = \frac{\tau_W}{0.5\rho U_{ref}^2} \tag{24}$$

The Nusselt number profiles shown in Figure 6 highlight how viscous dissipation influences heat transfer along the moving upper wall under forced convection (Ri = 0.1). For Ec = 0, the behavior is monotonic and physically intuitive: the Nusselt number begins at a high value of approximately 35.2 near the left corner, then continuously decreases toward the right wall, eventually reaching about 1.5. This steady decline corresponds to the growth of the thermal boundary layer along the lid, which reduces the temperature gradient at the wall and therefore diminishes the local heat transfer rate. The smooth, monotonic trend reflects the absence of internal heat generation, so the heat transfer is governed solely by convection and conduction.

When the Eckert number increases to Ec = 0.5, the profile becomes significantly more complex. The Nusselt value begins at about 47.0 and initially rises, reaching a local peak of 55.7 near x = 0.05. This early enhancement is due to the viscous dissipation within the thin high-shear region near the lid, which injects additional energy and steepens the thermal gradient at the wall. After this peak, the Nusselt number decreases gradually to 25.3 at x = 0.78, indicating a region where the heating effect becomes weaker relative to boundary-layer growth. Interestingly, the curve rises again to 29.9 near x = 0.95, suggesting a secondary zone of intensified shear or recirculation before a final rapid drop to 18.3 at the right boundary. The non-monotonic behavior reflects the interplay between local shear stress distribution and internal heat generation.

For Ec = 1, viscous dissipation becomes even more dominant, amplifying the non-monotonic pattern seen previously. The Nusselt number starts at 42.5, then sharply increases to a much larger peak of 64.5 around x = 0.1, indicating strong internal heating where shear is highest.

Afterward, the value decreases to 34.2 by x = 0.70, reflecting the weakening of thermal gradients where the boundary layer thickens. As with Ec = 0.5, the Nusselt number rises again near the right side, reaching 53.3 at x = 0.95—an effect likely caused by intensified flow curvature or vortex interactions close to the corner—before dropping rapidly to 34.2 at the right boundary. The increased amplitude and sharper transitions compared to Ec = 0.5 clearly demonstrate the strong thermal impact of viscous dissipation.

Overall, increasing the Eckert number transforms the heat-transfer behavior from a simple monotonic decay into a highly structured and oscillatory distribution. These oscillations correspond to zones where internal heating temporarily counteracts the natural thickening of the thermal boundary layer. At higher Ec, viscous dissipation becomes comparable to boundary-imposed heating, causing sharp enhancements and localized peaks in the Nusselt number. This highlights that even under forced convection, viscous heating can significantly alter the local wall heat transfer profile when Ec approaches order unity.

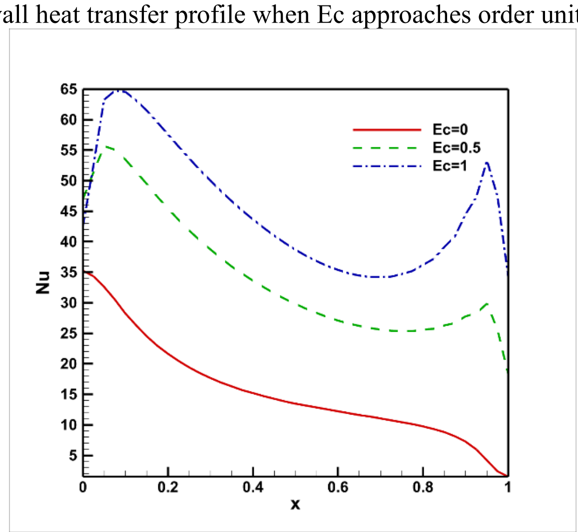

Fig. 6. Local Nusselt number distribution on the moving lid for different Eckert numbers at forced convection (Re = 100, Gr = 1000)

The Nusselt number distribution in Figure 7 represents mixed convection conditions with Re = 100 and Gr = 10000, corresponding to a Richardson number of approximately Ri = 1. Under Ec = 0, the Nusselt number begins at 43.7 on the left side of the moving lid and decreases smoothly and monotonically to about 2.2 at the right wall. This behavior is consistent with the simultaneous influence of forced and buoyancy-driven flow. Although the trend resembles the forced-convection case of Figure 6, the heat transfer values are notably higher due to the contribution of natural convection, which strengthens the upward thermal transport and increases the initial wall temperature gradient. The steady decline toward the right side again reflects boundary-layer thickening, but with a more amplified thermal field compared to the purely forced convection regime.

When the Eckert number increases to Ec = 0.5, the behavior becomes more complex, following the same qualitative pattern observed in Figure 6 but with noticeably larger amplitudes. The Nusselt number starts at 55.8 and rises to a peak of 63.5 near x = 0.05, indicating intensified viscous heating in the high-shear region close to the left corner. After this peak, the curve decreases to 25.3 at x = 0.78. As in the forced-convection case, a secondary rise occurs near x = 0.95 (reaching 27.0) before a final drop to 19.0 at the right boundary. Compared to Figure 6, the entire profile is shifted upward due to buoyancy effects, and the non-monotonic oscillations become somewhat more pronounced because natural convection enhances the redistribution of dissipated energy.

For Ec = 1, viscous dissipation becomes a dominant mechanism, leading to strong amplification of the Nusselt number throughout the lid. The curve starts at a very high value of 74.7 and quickly rises to 92.1 near x = 0.05—substantially larger than the peak of 64.5 observed in the forced-convection case. This dramatic increase demonstrates how buoyancy boosts the effect of viscous heating by promoting stronger recirculation and mixing, which steepens the temperature gradient at the wall. After this peak, the Nusselt number decreases to 40.7 at x = 0.75, followed by a secondary increase to 54.8 near x = 0.95, before dropping to 35.5 at the right wall. These oscillations are larger and more pronounced than those in Figure 6, confirming that viscous dissipation interacts more strongly with natural-convection flow structures.

Overall, Figure 7 shows that under mixed convection, both natural and forced mechanisms contribute to shaping the heat-transfer behavior, and the Eckert number's influence is more intense than in the purely forced convection case. As Gr increases, buoyancy strengthens the recirculating cells and enhances the ability of viscous dissipation to elevate local temperatures and steepen thermal gradients. Consequently, all Nusselt values shift upward, peaks become sharper, and the non-monotonic patterns observed on the lid become more pronounced. This comparison clearly demonstrates that the thermal impact of viscous heating grows significantly as the flow regime transitions from forced convection (Ri = 0.1) to mixed convection (Ri = 1).

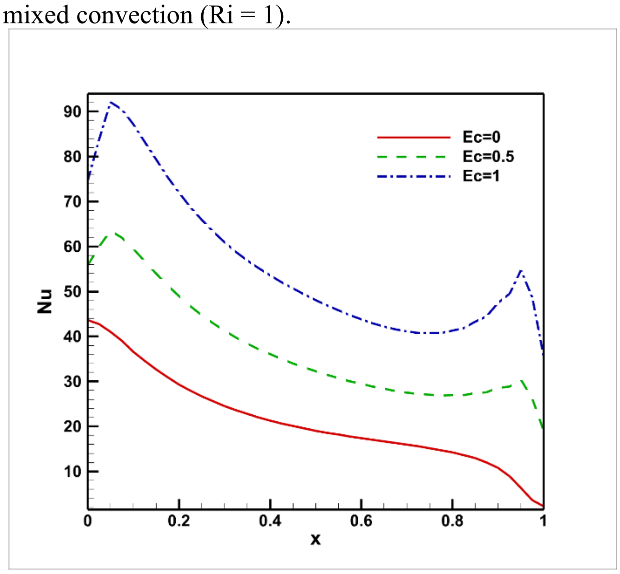

Fig. 7. Local Nusselt number distribution on the moving lid for different Eckert numbers at mixed convection (Re = 100, Gr = 10000)

Figure 8 presents the local Nusselt number distribution on the moving lid under free convection conditions (Re = 100, Gr = 100000), which implies a very high Richardson number (Ri >> 1), meaning buoyancy effects are dominant. For Ec = 0, the Nusselt number starts at 35.0 on the left and decreases non-linearly to 2.4 at the right wall. This monotonic decrease is characteristic of free convection boundary layers, where heat transfer generally diminishes as the thermal boundary layer grows along the surface. The values are comparable to the initial state of forced convection (Ec=0 in Fig. 6) but are higher than the corresponding free convection case in Figure 7 (Ec=0, Gr=10000) at the left edge (35.0 vs 43.7), suggesting a complex interplay of Gr and Re in determining the initial heat transfer. However, the clear monotonic decline in this free convection scenario with no forced flow contribution suggests that buoyancy-driven flow is the primary driver of heat transfer, with the boundary layer growing from left to right.

In stark contrast to the previous figures, the profiles for Ec = 0.5 and Ec = 1 in Figure 8 exhibit a single, pronounced peak, rather than multiple local maxima. For Ec = 0.5, the Nusselt number starts at 55.1 and increases dramatically to a high peak of 119.4 at x = 0.95, before dropping sharply to 93.4 at the right wall. This behavior is significantly different from the mixed convection case (Fig. 7), where the peak was much earlier and followed by a decrease and a smaller secondary rise. The late, sharp peak in free convection indicates that viscous dissipation becomes extremely effective in generating heat and steepening the thermal gradient only in the region very close to the right corner. This suggests that in free convection, the flow near the start might be less influenced by viscous dissipation, or the boundary layer grows so much that the effect only becomes dominant in the outer regions.

The trend is amplified for Ec = 1, where the Nusselt number begins at 52.1, increases to a massive peak of 168.6 at x = 0.98, and then falls to 159.6 at the right wall. This extreme peak highlights the tremendous impact of viscous dissipation in a buoyancy-dominated flow. The significant increase in Nusselt number as Ec goes from 0.5 to 1, and the fact that the peak occurs so late in the flow, suggest that in free convection, the combined effects of buoyancy and viscous heating create a very strong thermal gradient right at the end of the lid. This is a key difference from the earlier figures, where the peaks for Ec = 0.5 and Ec = 1 were observed much earlier (around x=0.05 to 0.1). The single, dominant peak in these free convection cases implies a more uniform influence of buoyancy across most of the lid, with viscous dissipation becoming critically important only in the very last part of the surface.

Comparing all three figures, we observe a clear progression: forced convection shows complex oscillations with Ec, mixed convection amplifies these oscillations and shifts them, while free convection, especially at higher Ec, leads to a single, extremely sharp peak near the end of the lid. This indicates that the relative importance of buoyancy versus forced flow, and the magnitude of viscous dissipation, fundamentally alter the local heat transfer characteristics. The transition from monotonic decay (Ec=0) to complex oscillations (forced convection) and finally to a single, sharp peak (free convection at high Ec) underscores the intricate coupling between flow dynamics and thermal transport under varying convection regimes.

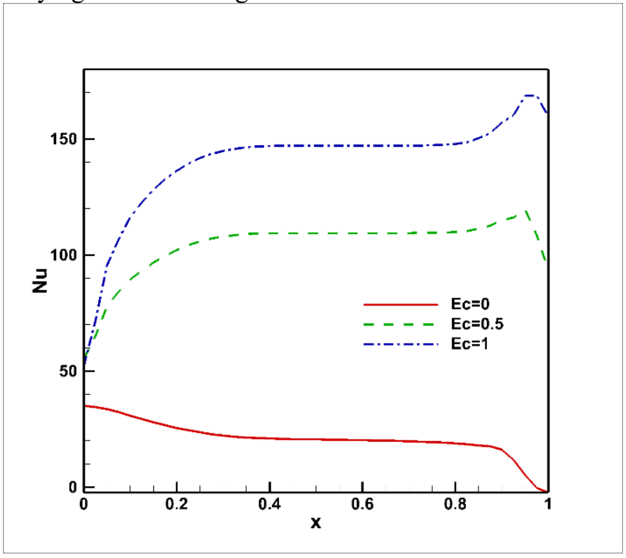

Fig. 8. Local Nusselt number distribution on the moving lid for different Eckert numbers at free convection (Re=100, Gr=100000)

The friction factor, presented here as its local distribution on the moving lid, is a key metric for quantifying pressure drop and energy loss due to shear forces in fluid flow. In engineering applications, understanding and controlling the friction factor is crucial for optimizing system performance, reducing energy consumption, and preventing equipment wear. This factor depends on parameters such as the Reynolds number (Re), Grashof number (Gr), flow geometry, and fluid properties, including the effects of viscous dissipation (represented by the Eckert number, Ec).

Figure 9 illustrates the local friction factor distribution on the moving lid for three different Eckert numbers (0, 0.5, and 1) under forced convection conditions (Re=100, Gr=1000). In all three cases, the friction factor begins at an initial value of 1.24 at the left edge, decreases monotonically, and reaches its minimum value of 0.18 around x=0.60. Subsequently, the friction factor increases again, returning to 1.24 at the right edge. While the distribution is not perfectly symmetrical, it is close to symmetrical. This behavior indicates that the highest shear stress occurs at the initial and final regions of the moving lid, with the minimum occurring in the middle.

A notable observation from these results is the lack of significant influence from the Eckert number on the friction factor distribution. As you pointed out, the differences between Ec = 0, Ec = 0.5, and Ec = 1 are minimal, with the profiles nearly overlapping. This implies that within this specific flow regime (forced convection with Re=100 and Gr=1000), the effect of viscous dissipation on shear stress, and consequently on the friction factor, is negligible compared to the effects arising from the Reynolds number and flow geometry. This finding aligns with some theoretical studies that suggest viscous dissipation effects become more pronounced at higher velocities (high Re) or very large Eckert numbers. In these particular conditions, the energy dissipated by viscosity is not substantial enough to significantly alter the shear stress distribution.

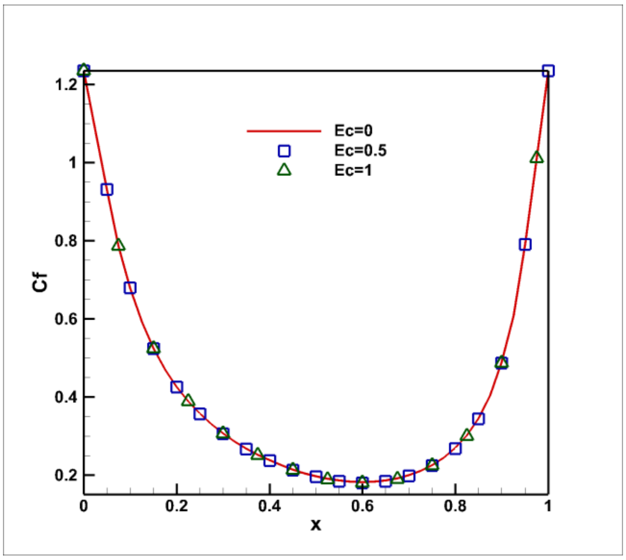

Fig. 9. Friction factor distribution on the moving lid for different Eckert numbers at forced convection (Re=100, Gr=1000)

Figure 10 presents the local friction factor distribution along the moving lid for different Eckert numbers (Ec = 0, 0.5, and 1) under mixed convection conditions (Re = 100, Gr = 10000). For Ec = 0, the friction factor starts at about 1.24 near the left edge, decreases gradually, reaches a minimum of approximately 0.19 at x = 0.65, and then increases again to about 1.24 near the right edge. Although the profile is not perfectly symmetric, it remains close to symmetric, and the general shape (decrease–minimum–increase) is consistent with the same trend across the three Ec values. For Ec = 0.5 and Ec = 1, you observe almost the same results, with only very small deviations that would become visible if the data were reported with higher precision (e.g., to three decimal places).

Comparison with Figure 9 and interpretation

Comparing Figure 10 with Figure 9 (Re = 100, Gr = 1000), the overall behavior of the friction factor profile is remarkably similar in both cases: the friction factor begins at ~1.24, drops to a minimum around x ≈ 0.60–0.65, and returns to ~1.24 toward the right side, with Eckert number having little influence on the macroscopic shape. Even though Gr increases from 1000 to 10000 (which intensifies buoyancy effects), the friction-factor distribution still appears dominated by the flow driven by the lid motion and the associated shear/velocity structure. Hence, in this regime, the additional viscous dissipation effects represented by Ec do not significantly alter the near-lid shear distribution; instead, the friction factor remains primarily controlled by Re and the flow geometry, while changes due to Ec are secondary and only detectable at very small levels.

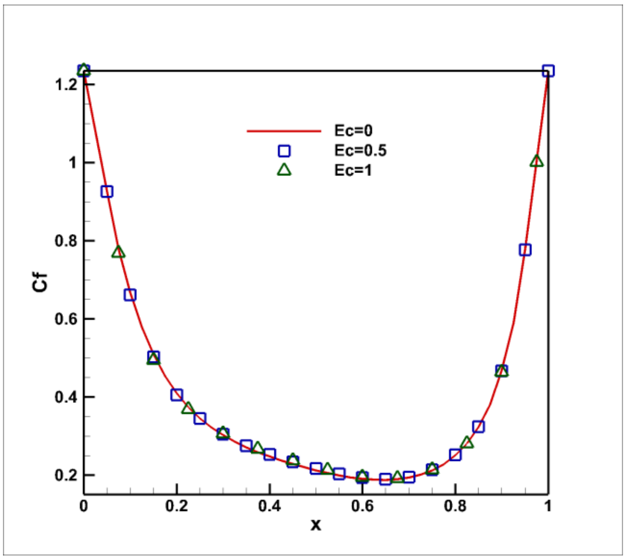

Fig. 10. Friction factor distribution on the moving lid for different Eckert numbers at mixed convection (Re=100, Gr=10000)

Figure 11 illustrates the local friction factor distribution along the moving lid under free convection conditions (Re=100, Gr=100000) for Eckert numbers of 0, 0.5, and 1. At Ec=0, the friction factor starts at 1.24 on the left edge, gradually decreases, reaches a minimum of 0.05 at x=0.73, and then increases back to 1.24 on the right edge. While not perfectly symmetrical, the profile is nearly so. When the Eckert number increases to 0.5, a significant change in the friction factor profile is observed: its minimum value rises to 0.30 at x=0.63, and a region with a near-zero slope (where the friction factor changes by less than 10% from x=0.33 to x=0.85) emerges. This trend continues for Ec=1, with a minimum value of 0.31 at x=0.63. The difference between Ec=0.5 and Ec=1 is very small, whereas both show a considerable deviation from the Ec=0 case.

Comparing the three figures depicting the friction factor distribution across different convection regimes reveals substantial changes. In Figure 9 (forced convection, Gr=1000) and Figure 10 (mixed convection, Gr=10000), the friction factor is barely affected by the Eckert number, resulting in nearly identical profiles. The minimum friction factor values in these two cases are approximately 0.18 and 0.19, respectively. However, in Figure 11 (free convection, Gr=100000), with the dominance of free convection (higher Grashof number), the influence of the Eckert number becomes much more pronounced. Here, the Eckert number not only significantly increases the minimum friction factor (from 0.05 to about 0.30-0.31) but also creates a flattened, low-gradient region in the central part of the plot. This indicates that as buoyancy effects (increased Gr) and viscous dissipation (increased Ec) become more significant, the mechanisms of shear stress transfer near the moving wall are altered, leading to a transformed friction factor behavior.

Comparison of Nusselt Number Variations with Friction Factor Changes Across the Last Six Figures

A comparison of the Nusselt number (Nu) and friction factor (Cf) distributions across the last six figures reveals interesting correlations. In Figures 6 and 7 (free convection, Re=100, Gr=100000 and Gr=0), the Nusselt number increases sharply with the Eckert number (Ec), particularly near the right wall. This significant rise in Nu aligns with the pronounced effect of Ec on the temperature profiles. Conversely, in these figures, the friction factor (Cf) also changes under the influence of Ec, but its pattern does not perfectly mirror that of Nu. In Figure 8 (free convection, Re=100, Gr=100000, Ec=0), Nu was decreasing, and f exhibited a decrease-increase behavior. However, with increasing Ec in the same conditions (Figure 8 with Ec>0), Nu develops a very sharp peak near the right wall, while f also increases in that region, though not as dramatically as Nu.

In Figures 9 and 10 (forced and mixed convection), both Nu and f show very little influence from Ec, and their profiles remain largely constant. This suggests that in these regimes, the dominant heat transfer and shear stress mechanisms are dictated by Re, and the effects of viscous dissipation and buoyancy (up to these levels) are less significant.

Finally, Figure 11 (free convection, Re=100, Gr=100000) marks a turning point. Here, with the prevalence of free convection, Ec significantly impacts both Nu and f. An increase in Ec leads to a substantial rise in Nu (similar to Figure 8 with Ec>0) and also causes a notable increase in the minimum f value and a change in its distribution pattern. In general, it can be concluded that in the free convection regime (high Gr), increasing Ec affects both heat transfer (Nu) and energy dissipation (Cf). In contrast, in the forced and mixed convection regimes (lower Gr), these effects are considerably diminished, with Re playing the dominant role.

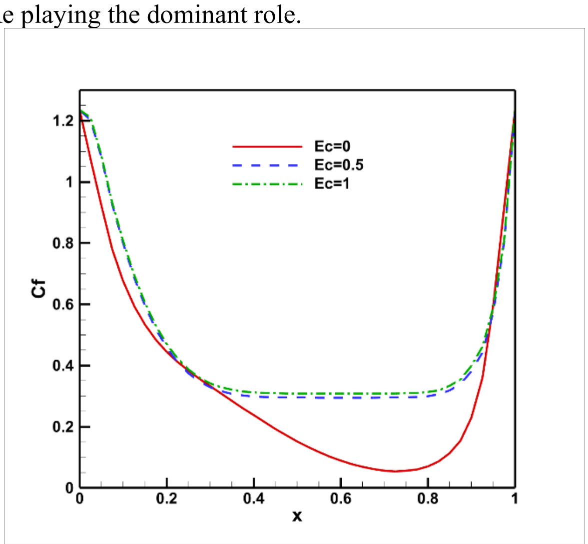

Fig. 11. Friction factor distribution on the moving lid for different Eckert numbers at free convection (Re=100, Gr=100000)

Table 1 presents the trend of the mean Nusselt number (Nu_{av}) across different convection types and Eckert numbers (Ec). In all three convection regimes (forced, mixed, and free), the mean Nusselt number significantly increases as the Eckert number rises from 0 to 0.5 and then to 1. This elevation signifies the crucial role of viscous dissipation in heat transfer; as Ec increases, more energy is lost due to friction within the fluid, converting into heat. This, in turn, raises the fluid temperature and consequently enhances heat transfer. Notably, the increase in Nu with rising Ec is far more pronounced in free convection (from 20.95 to 103.95 and then to 139.89) compared to the other two regimes (from 15.55 to 34.47 and 45.20 for forced convection, and from 21.28 to 37.32 and 56.09 for mixed convection). This observation confirms that under dominant free convection conditions, the impact of viscous dissipation on heat transfer becomes substantially more significant.

Examining the mean friction factor (f_{av}) columns in Table 1 reveals different trends compared to the Nusselt number. In both forced convection ($Gr=10^3$) and mixed convection ($Gr=10^4$) scenarios, the mean friction factor remains nearly constant, exhibiting negligible variations (around 0.430 and 0.426, respectively). This stability supports the earlier findings from Figures 9 and 10, indicating that changes in the Eckert number have a minimal effect on the overall wall shear stress in these regimes. However, in the free convection case ($Gr=10^5$), the mean friction factor increases substantially as the Eckert number rises from 0 to 0.5 and 1, going from 0.358 to 0.471 and then to 0.483. This significant rise in fav under free convection and with increasing Ec suggests a change in the flow's fundamental characteristics and an increase in energy dissipation near the moving wall, correlating with more pronounced changes in velocity profiles and shear stress.

Overall Trend Comparison and Correlation between Nu_{av} and f_{av}

A holistic comparison of Table 1 highlights that in forced and mixed convection regimes, the Eckert number primarily influences heat transfer, leading to a considerable boost in Nu_{av}, while fav remains largely unchanged. This implies that in these conditions, the added energy from viscous dissipation effectively contributes to heat transfer without substantially altering the overall shear stress. In contrast, under free convection, both Nu_{av} and fav are significantly affected by changes in Ec. The simultaneous increase in both Nu_{av} and fav in this scenario indicates that viscous dissipation not only enhances heat transfer but also contributes to increased energy dissipation and shear stress within the fluid. This distinct behavior in free convection arises from the dominance of buoyancy effects, creating a more intricate interplay between temperature, velocity, and shear stress.

Table 1
Mean Nusselt number and friction factor for different types of convection at Re = 100 and varying Eckert numbers

	Ec = 0		Ec = 0.5		Ec = 1	
	Nu_{av}	f_{av}	Nu_{av}	f_{av}	Nu_{av}	f_{av}
Forced convection ($Re=100, Gr=10^3$)	15.55	0.430	34.47	0.429	45.20	0.434
mixed convection ($Re=100, Gr=10^4$)	21.28	0.426	37.32	0.426	56.09	0.425
free convection ($Re=100, Gr=10^5$)	20.95	0.358	103.95	0.471	139.89	0.483

4. CONCLUSION

This research comprehensively investigated the influence of the Eckert number (Ec) on the mean Nusselt number (Nu_{av}) and mean friction factor (f_{av}) across forced, mixed, and free convection regimes, as detailed in Table 1. Our findings quantitatively demonstrate that viscous dissipation significantly enhances heat transfer, with Nu_{av} escalating notably as Ec increases from 0 to 0.5 and then to 1. For instance, in free convection, Nu_{av} rose dramatically from 20.95 to 103.95 and further to 139.89, underscoring the substantial role of frictional heat generation. Conversely, in forced convection, Nu_{av} showed a more moderate increase from 15.55 to 45.20 over the same Ec range.

A key distinction emerged in the behavior of the mean friction factor. While f_{av} remained relatively stable in forced (around 0.430) and mixed convection (around 0.426) as Ec varied, free convection presented a different dynamic. Here, fav exhibited a marked increase from 0.358 at Ec=0, to 0.471 at Ec=0.5, and reaching 0.483 at Ec=1. This suggests that in free convection, viscous dissipation not only boosts heat transfer but also intensifies flow resistance and energy dissipation within the fluid. The observed trends highlight that the dominance of buoyancy effects in free convection leads to a more intricate coupling between thermal and hydrodynamic behaviors under the influence of viscous dissipation, a phenomenon less pronounced in forced or mixed convection where inertial forces play a larger role.

Building upon these findings, several avenues warrant further exploration. Future research could delve into the impact of varying Grashof numbers (Gr) in conjunction with a wider range of Eckert numbers to map the boundaries of these distinct behaviors more precisely. Investigating the effects of different fluid properties, such as Prandtl number, on the Nu_{av} and f_{av} correlations under high Ec conditions would also be valuable. Furthermore, extending this analysis to three-dimensional flow scenarios or exploring the transient behavior of these parameters during the onset of convection with significant viscous dissipation could provide deeper insights for advanced thermal management applications. The development and validation of more sophisticated computational models capable of accurately capturing these complex interactions at high Eckert numbers would also be a significant contribution.

REFERENCES

[1] M. Nawaz, "Numerical study of hydrothermal characteristics in nano fluid using KKL model with Brownian motion," (in en), *Scientia Iranica,* vol. 26, no. 3, pp. 1931-1943, 2019, doi: 10.24200/sci.2019.50073.1494.

[2] N. Amar and N. Kishan, "The influence of radiation on MHD boundary layer flow past a nano fluid wedge embedded in porous media," *Partial Differential Equations in Applied Mathematics,* vol. 4, p. 100082, 2021/12/01/ 2021, doi: https://doi.org/10.1016/j.padiff.2021.100082.

[3] T. Gong and Y. Wang, "An artificial neural network-based quadratic constitutive Reynolds stress model for separated turbulent flows using data-augmented field inversion and machine learning," *Physics of Fluids,* vol. 37, no. 3, p. 035153, 2025, doi: 10.1063/5.0263211.

[4] T. Adibi and S. E. Razavi, "A Data-Driven Physics-Informed Neural Network for Correcting Structural Errors in RANS Turbulence Models," (in en), *Computational Sciences and Engineering,* 2026, doi: 10.22124/cse.2026.32957.1159.

[5] M. A. Jamil, N. Imtiaz, K. C. Ng, B. B. Xu, H. Yaqoob, M. Sultan, and M. W. Shahzad, "Experimental and parametric sensitivity analysis of a novel indirect evaporative cooler for greener cooling," *Thermal Science and Engineering Progress,* vol. 42, p. 101887, 2023/07/01/ 2023, doi: https://doi.org/10.1016/j.tsep.2023.101887.

[6] N. V. K, "Opportunities, challenges, and state of the art of flexible heat-pipe heat exchangers: A comprehensive review," *Heat Transfer,* vol. 53, no. 2, pp. 893-938, 2024/03/01 2024, doi: https://doi.org/10.1002/htj.22978.

[7] M. H. Shojaeefard and S. Saremian, "Analyzing the impact of blade geometrical parameters on energy recovery and efficiency of centrifugal pump as turbine installed in the pressure-reducing station," *Energy,* vol. 289, p. 130004, 2024/02/15/ 2024, doi: https://doi.org/10.1016/j.energy.2023.130004.

[8] X. Liang, M. Min, K. Bian, and J. Cheng, "Study on the enhanced heat transfer and exergy performance of the finned tube heat exchanger with vortex generator," *International Journal of Thermal Sciences,* vol. 210, p. 109639, 2025/04/01/ 2025, doi: https://doi.org/10.1016/j.ijthermalsci.2024.109639.

[9] R. D. Alsemiry, H. M. Sayed, and N. Amin, "Mathematical analysis of Carreau fluid flow and heat transfer within an eccentric catheterized artery," *Alexandria Engineering Journal,* vol. 61, no. 1, pp. 523-539, 2022/01/01/ 2022, doi: https://doi.org/10.1016/j.aej.2021.06.029.

[10] S. Shukla, R. P. Sharma, T. M. Agbaje, and S. Mondal, "Investigation of thermodynamics characteristics of ternary hybrid nanofluid flow over a stretching sheet," *Modern Physics Letters B,* vol. 38, no. 12, p. 2450079, 2024/04/30 2023, doi: 10.1142/S0217984924500799.

[11] C. M. Mohana and B. R. Kumar, "Numerical and semi-analytical approaches for heat transfer analysis of ternary hybrid nanofluid flow: A comparative study," *Mathematics and Computers in Simulation,* vol. 226, pp. 66-90, 2024/12/01/ 2024, doi: https://doi.org/10.1016/j.matcom.2024.06.019.

[12] T. A. Seyed Esmail Razavi , Hussein Hassanpour, " Thermo-flow Analysis of Cylinder with Crossed Splitter Plates with a Characteristics-based Scheme," *International Journal of Thermodynamics,* vol. 24, no. 2, pp. 83-91, 2021, doi: 10.5541/ijot.783614.

[13] T. Adibi, S. E. Razavi, S. F. Ahmed, S. C. Saha, and N. A. Shah, "Role of a Hinged Single Separator in Heat Transfer Enhancement and Drag Reduction in Circular Cylinder Flow," *Arabian Journal for Science and Engineering,* 2024/08/18 2024, doi: 10.1007/s13369-024-09435-2.

[14] T. Adibi, S. E. Razavi, S. F. Ahmed, S. M. Shakor, and G. Liu, "Effects of Elastic Walls on the Thermal Performance of a Counterflow Heat Exchanger," *International Journal of Energy Research,* vol. 2024, no. 1, p. 8895936, 2024/01/01 2024, doi: https://doi.org/10.1155/er/8895936.

[15] N. Hedayati and A. Ramiar, "Investigation of two phase unsteady nanofluid flow and heat transfer between moving parallel plates in the presence of the magnetic field using GM," (in en), *Challenges in Nano and Micro Scale Science and Technology,* vol. 4, no. 1, pp. 52-58, 2016, doi: 10.7508/tpnms.2016.01.007.

[16] S. M. Ibrahim, p. Vijaya Kumar, and C. S. K. Raju, "Possessions of viscous dissipation on radiative MHD heat and mass transfer flow of a micropolar fluid over a porous stretching sheet with chemical reaction," (in en), *Challenges in Nano and Micro Scale Science and Technology,* vol. 6, no. 1, pp. 60-71, 2018, doi: 10.22111/tpnms.2018.3523.

[17] G. A. Sheikhzadeh, A. Aghaei, and S. soleimani, "Effect of nanoparticle shape on natural convection heat transfer in a square cavity with partitions using water-SiO2 nanofluid," (in en), *Challenges in Nano and Micro Scale Science and Technology,* vol. 6, no. 1, pp. 27-38, 2018, doi: 10.22111/tpnms.2018.3520.

[18] A. Shahriari, "Lattice Boltzmann method for MHD natural convection of CuO/water nanofluid in a wavy-walled cavity with sinusoidal temperature distribution," (in en), *Challenges in Nano and Micro Scale Science and Technology,* vol. 5, no. 2, pp. 111-129, 2017, doi: 10.7508/tpnms.2017.02.005.

[19] A. A. Abbasian Arani, M. Abbaszadeh, and A. Ardeshiri, "Mixed convection fluid flow and heat transfer and optimal distribution of discrete heat sources location in a cavity filled with nanofluid," (in en), *Challenges in Nano and Micro Scale Science and Technology,* vol. 5, no. 1, pp. 30-43, 2016, doi: 10.7508/tpnms.2017.01.004.

[20] R. P. Sharma, P. K. Pattnaik, S. R. Mishra, S. Tinker, and S. R. Allipudi, "Enhancing heat transfer on the free convection of conducting hybrid nanofluid through stretching/shrinking surface," *Pramana,* vol. 98, no. 3, p. 96, 2024/07/11 2024, doi: 10.1007/s12043-024-02762-x.

[21] R. P. Sharma, S. Baag, S. R. Mishra, and P. Sahoo, "Illustration of thermal radiation on the mixed convection of Williamson nanofluid over an inclined cylindrical surface," *Modern Physics Letters B,* vol. 38, no. 25, p. 2450141, 2024/09/10 2024, doi: 10.1142/S0217984924501410.

[22] Z. Iqbal *et al.*, "Thermal convection and entropy generation analysis of hybrid nanofluid slip flow over a horizontal poignant thin needle with an inclined magnetic field: A numerical study," *Modern Physics Letters B,* vol. 38, no. 05, p. 2450004, 2024/02/20 2023, doi: 10.1142/S0217984924500040.

[23] S. E. Razavi, T. Adibi, and H. Hassanpour, "Sensitivity Analysis on Thermal Performance of Gas Heater with Finned and Finless Tubes using Characteristics-based Method," (in en), *International Journal of Engineering,* vol. 34, no. 6, pp. 1537-1544, 2021, doi: 10.5829/ije.2021.34.06c.18.

[24] T. Adibi, S. E. Razavi, O. Adibi, M. Vajdi, and F. Sadegh Moghanlou, "The response of nano-ceramic doped fluids in heat convection models: A characteristics-based numerical approach," (in en), *Scientia Iranica,* vol. 28, no. 5, pp. 2671-2683, 2021, doi: 10.24200/sci.2021.56574.4794.

[25] S. E. Razavi and T. Adibi, "Simulation of fluid flow in a counter-flow heat exchanger with partly elastic intermediate walls," (in en), *Computational Sciences and Engineering,* 2026, doi: 10.22124/cse.2026.32640.1149.

[26] T. Adibi and S. E. Razavi, "A novel multidimensional characteristic modeling of incompressible convective heat transfer," (in en), *Journal of Solid and Fluid Mechanics,* vol. 5, no. 4, pp. 283-296, 2015, doi: 10.22044/jsfm.2015.683.

[27] S. E. Razavi and T. Adibi, "A novel multidimensional characteristic modeling of incompressible convective heat transfer," *Journal of Applied Fluid Mechanics,* vol. 9, no. 4, pp. 1135-1146, 2016 2016, doi: 10.18869/acadpub.jafm.68.228.24295.

[28] T. Adibi and S. E. Razavi, "A new characteristic approach for incompressible thermo-flow in Cartesian and non-Cartesian grids," *International Journal for Numerical Methods in Fluids,* vol. 79, no. 8, pp. 371-393, 2015, doi: 10.1002/fld.4053.

[29] R. Iwatsu, J. M. Hyun, and K. Kuwahara, "Mixed convection in a driven cavity with a stable vertical temperature gradient," *International Journal of Heat and Mass Transfer,* vol. 36, no. 6, pp. 1601-1608, // 1993, doi: http://dx.doi.org/10.1016/S0017-9310(05)80069-9.